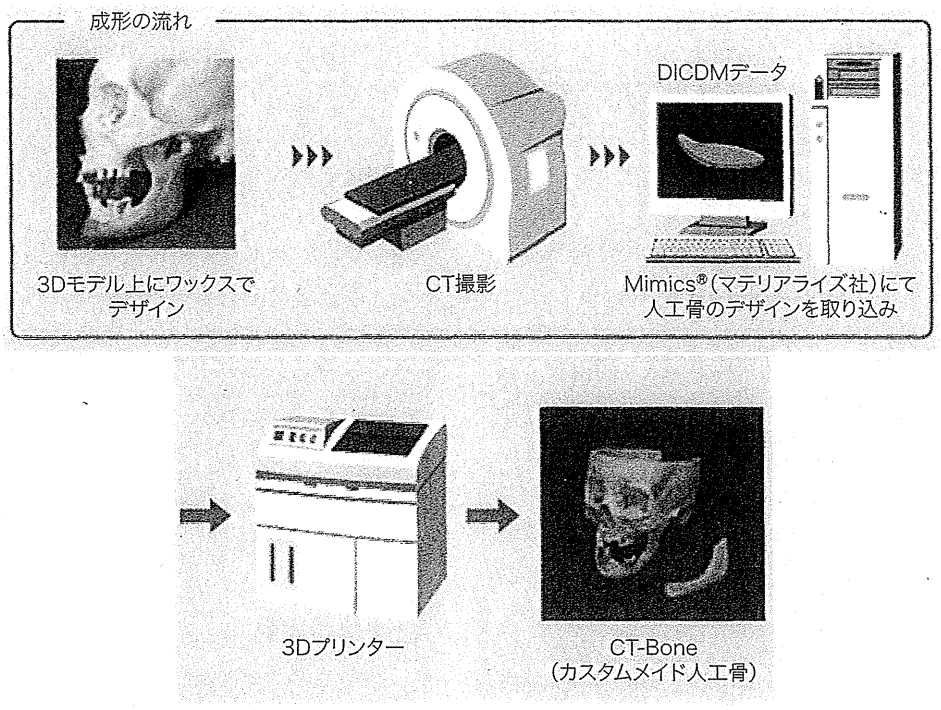

図 1　カスタムメイド型人工骨（CT-Bone）の作製過程
患者の欠損部に適合する人工骨を作製するため，まず，それぞれの患者の 3D 石膏モデル上で，ワックスを用いて人工骨のデザインを形成する。CT を撮影し，形成したワックス部分の形状を DICOM データとして取り込み，3D インクジェットプリンタを用いて CT-Bone を作製する。
（文献 16 から引用）

tor：PDGF）[12]などを用いた検討もなされている。

顎骨の再生

比較的大型な顎骨欠損に対しては，遊離骨移植や血管柄付き骨移植などの再建術が適応となる。安定した治療実績をもつ術式ではあるが，複雑な形態を有する顎顔面領域で，審美的に十分に満足がいく再建を行うことは難しく，採骨部への侵襲性も低くはない。再生医療の導入が有用になると考えられるが，歯周病などに起因する歯槽骨欠損とは欠損の大きさにも違いがあり，再生医療によるアプローチもその分ハードルが高くなる。

再生医療の概念を利用した治療法として，近年，腸骨から採取した骨髄海綿骨（particulate cancellous bone and marrow：PCBM）とチタンメッシュトレーによる骨再建法が多用されている。この方法では，トレーを適切に整形することにより，より自然な形態修復が可能であり，義歯やインプラントなどを併用した良好な咬合回復も期待できる。移植骨そのものの生着を目的とした従来の骨移植とは異なり，PCBM 移植は生体に備わった骨形成能を引き出すことを目的とした，いわゆる *in situ* tissue engineering である[13]。小下顎症の治療などで用いられる骨延長術も，骨切り部が治癒する過程で生じる仮骨をゆっくりと牽引することにより骨形成を誘導する治療法であり，*in situ* tissue engineering に基づく方法であるといえる。

足場素材のみを用いた骨再生としては，ハイドロキシアパタイトなどのリン酸カルシウム系の骨補塡材がある。特にβリン酸三カルシム（βTCP）は，移植後の生体内で徐々に吸収され，骨に置換されていくため，よく用いられる。cm 単位の大きな欠損に使用されることもあるが，血行が付与されていないため感染には弱い。

名古屋大学の日比らのグループは，自己骨髄由来の骨形成性細胞に多血小板血漿，トロンビン，塩化カルシウムを組み合わせ，自家骨に代わる移

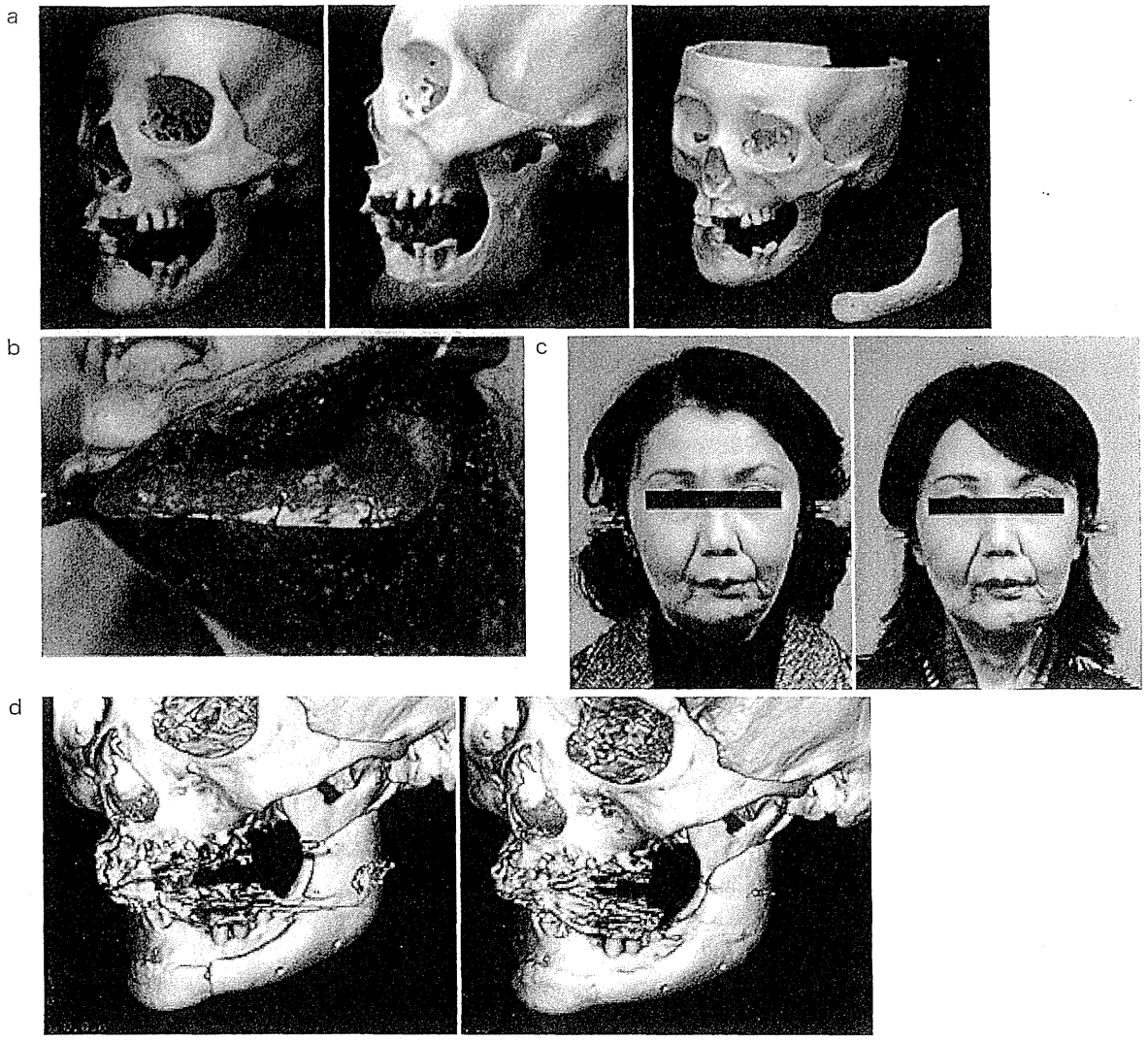

図 2　カスタムメイド型人工骨（CT-Bone）の臨床応用
a：3D 石膏模型上（左）で，CT-Bone のデザインをワックス形成した（中央）。CT を撮影したのち，ワックス部分の形状を DICOM データで取り込み，3D インクジェットプリンタを用いて CT-Bone を作製した（右）。
b：CT-Bone を移植した術中写真。
c：術前（左）および術後（右）の患者の顔貌写真。
d：術直後（左）および術後 2 年（右）の CT 所見。術後 2 年で，母床骨と CT-Bone との界面では骨癒合が観察された。
（文献 17 から引用）

植材料として顎骨の先天性欠損に応用している[14]。自家骨移植と遜色ない結果が得られてはいるが，下顎骨区域切除後のような大きな欠損での実績はない。

われわれは，本学 工学系研究科/医学系研究科 鄭雄一教授らと連携し，生体が元来有している骨形成能を最大限に引き出せるような人工骨の開発を検討してきた[15]。CT 画像から骨欠損・変形部位に適合するカスタムメイド型の人工骨（CT-Bone）を作製して移植する技術を確立し，複雑な顎顔面形態も容易に再現可能となった（**図 1**）[16]。先天異常，外傷，腫瘍切除などにより非荷重部位に顎顔面陥凹変形を有する患者を対象に，2006 年に CT-Bone の臨床研究を 10 例，2008～2009 年に治験を約 20 例行った（**図 2**）[17]。患者の CT 画像をもとに人工骨を作製するため，患部への適合も

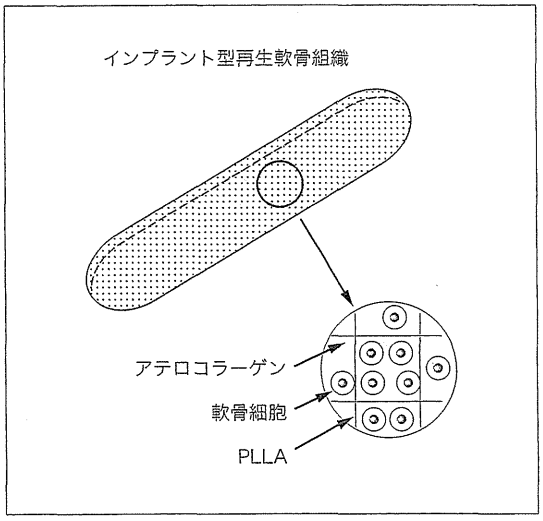

図 3　インプラント型再生軟骨の構成
インプラント型再生軟骨は，培養耳介軟骨細胞を PLLA 多孔体に投与して作製する。細胞が多孔体から漏れ出さないように，アテロコラーゲンを粘剤として使用する。長さ 5 cm，幅 6 mm，高さ 3 mm のドーム状の形状をしている。
（文献 16 から引用）

良好で，術者による形状調整がほぼ不要であった。また，十分に手術に耐えられる強度（20 MPa）を有しているため，優れた操作性を示すことも明らかとなった。これまでのところ安全面での問題はなく，人工骨と母骨との癒合も速やかに起こっていることが確認されている。使用において注意すべき点としては，移植時点では異物であるという点においてはほかの人工骨と差はなく，放射線照射野や感染部位に移植することは避けるべきであることも判明した。今後は荷重部への適応拡大をめざし，金属など他材料とのハイブリッド化や，骨誘導シグナルとの融合などによる高機能化人工骨を開発していく必要があると考え，研究開発を継続している。

粘膜の再生

癌切除後や先天異常などで生じる大きな粘膜欠損に対しては，植皮が行われることも多い。しかし粘膜と皮膚では表面性状に違いがあり，採取部の侵襲も避けられない。培養口腔粘膜の場合，角化細胞のみの上皮シートでは破れやすく，母床とも接着しにくいため，結合組織との 2 層構造を用いるほうが望ましいとされる。新潟大学の研究グループでは，ヒト無細胞性，非免疫原性新鮮屍体真皮 AlloDerm®（LifeCell, Branchburg, New Jersey）に自家口腔粘膜角化細胞を播種し，重層化させた全層口腔粘膜（EVPOME®）を開発し[18]，2000 年から臨床応用を開始している。EVPOME® は，無血清培養が可能であり，AlloDerm® で裏装されているため取り扱いやすく，血管新生も促進されやすいなどの特徴を有している。一方，近年のバイオマテリアルの進歩は著しく，ポリグリコール酸（polyglycolic acid：PGA）不織布およびフィブリノゲン製剤を用いた創傷被覆療法が，口腔粘膜再建の良好な臨床成績を収めている[19]。今後は，再生医療とバイオマテリアルを用いた再建治療の両者を上手に使い分け，それぞれの利点を生かす選択を行っていく必要があろう。

軟骨の再生と気管再生への応用

軟骨再生医療は，皮膚や角膜などとともに再生医療のなかでも比較的臨床応用が進んでいる領域で，自家軟骨細胞移植（autologous chondrocyte implantation：ACI）が，欧米を中心に医療として普及している。ACI 原法は，関節軟骨の局所的な欠損に対し，非荷重部の関節軟骨から軟骨細胞を単離し，培養増殖させたのちに細胞懸濁液として欠損部に投与し，さらに漏出を防ぐために骨膜パッチで被覆する。しかし，現行の軟骨再生医療は局所的な軟骨欠損の補塡を目的とするため，移植される細胞は液状あるいはゲル状であり，唇口蓋裂に伴う重度の鼻変形（唇裂鼻変形）などへの適応は困難である。そこでわれわれは，適切な強度と 3 次元形状を有する再生軟骨の開発に取り組み，患者由来の耳介軟骨細胞を 5% 自己血清，FGF-2（100 ng/mL），インスリン（5 μg/mL）を組み合わせた培養液で増殖させ，医療用具として使用実績のあるアテロコラーゲン® に懸濁し，ポリ乳酸（poly-L-lactic acid：PLLA）多孔性足場素材に播種して作製するインプラント型再生軟骨を開発した（図 3）[16,20]。前臨床試験において有効性と安全性を確認し，「ヒト幹細胞を用いる臨床研究

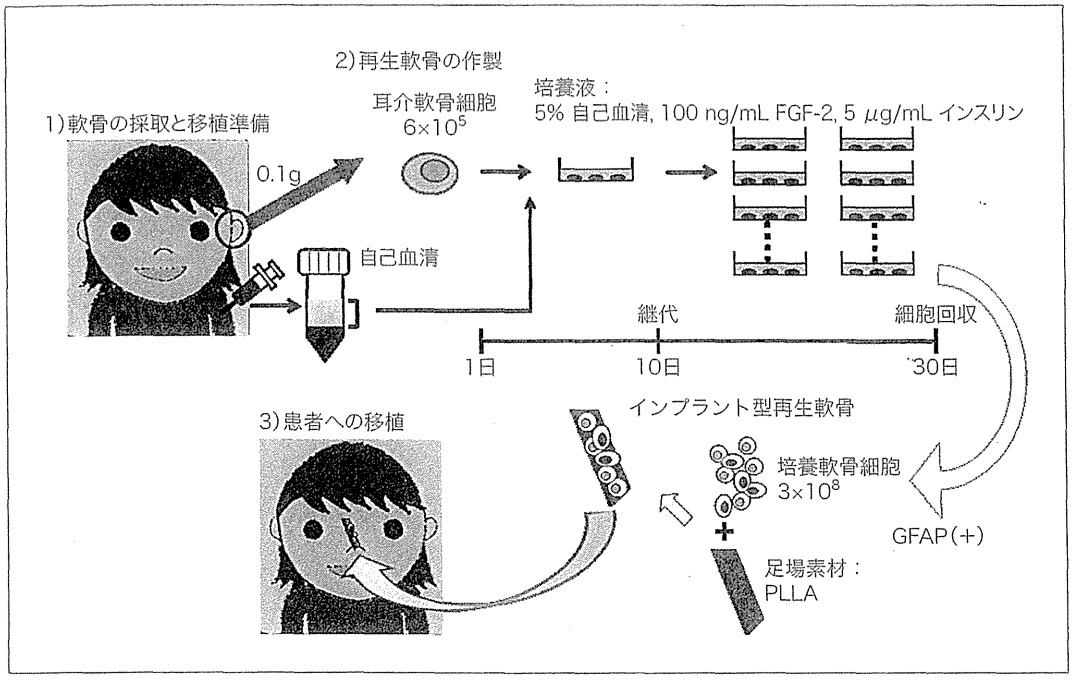

図 4　インプラント型再生軟骨の自主臨床研究プルトコール
再生軟骨の製造と治療の流れを示す。外来で自己血清を 400 mL 採取したのち，初回入院で耳介軟骨 0.1 g を採取するとともに，必要に応じて口唇鼻修正を追加した。そののち，東京大学病院細胞プロセッシングセンターで，採取した耳介組織から軟骨細胞を単離し，約 1 か月間培養増殖させた。2 回目の入院では，手術当日に回収した細胞を用いて再生軟骨を作製し，唇裂鼻変形を有する患者の鼻背に移植した（3 症例）。
（文献 16 から引用）

に関する指針」に基づき，安全性の確認を主要評価項目に，唇裂鼻変形の患者 3 名に対し自主臨床研究を行った（図 4）[20]。2011 年 7 月に 1 例目の患者に移植手術を行い，約 2 年半程度経過を観察しているが，すべての症例で抜去に至るような重大な有害事象もなく，経過良好である。今後は，東京医科歯科大学や山形大学と連携して，多施設臨床研究を実施する予定である。

インプラント型再生軟骨は，足場素材の形態を調整することにより目的とする 3 次元形態を付与することが可能であり，軟骨組織としての十分な力学的特性を有している。また，現在行っている自主臨床研究で，移植後にも安定した経過をたどることが確認されたことから，われわれはインプラント型再生軟骨の適応拡大，具体的には，気管や関節への応用を検討している。再生気管軟骨に関しては，気管狭窄症などの症例への移植を想定している。PLLA 多孔体部分に培養自己耳介軟骨細胞を播種して軟骨を再生させると同時に，PLLA 多孔体の内面に微細加工を施して，周囲組織からの粘膜再生を誘導したいと考えている。現在，ウサギやビーグル犬を用いた自家再生気管軟骨移植実験で，安全性および有効性の確認を行っている。

おわりに

歯科口腔外科の再生医療に関して，わが国で行われている試みを中心に概説した。口腔外科領域はさまざまな組織から構成されるため，再生医療の研究ターゲットも幅広い。また，紙面の都合上紹介できなかったが，歯髄幹細胞の神経再生効果なども報告されており[21]，再生医療における細胞源としても注目を集めている。

われわれのグループは長年にわたり，口蓋裂や小耳症の子どもたちの治療に携わってきた。小耳症の再建では，患者から採取した肋骨を，術者が耳介の形態へ細工していくという術式が施行され

ることが多いが，侵襲性，審美性の点からも，再生医療の導入が有用になると考えている。3次元造形を活用して作製された足場素材とiPS細胞を用いて，子どもたちに負担が少なく，かつ見た目にも満足がいく耳介再建が実現できるような日が来ることを，期待している。

文献

1) Langer R, et al：Tissue engineering. Science 260：920-926, 1993
2) Ikeda E, et al：Growing bioengineered teeth from single cells：potential for dental regenerative medicine. Expert Opin Biol Ther 8：735-744, 2008
3) Nakao K, et al：The development of a bioengineered organ germ method. Nat Methods 4：227-230, 2007
4) Ikeda E, et al：Fully functional bioengineered tooth replacement as an organ replacement therapy. Proc Natl Acad Sci U S A 106：13475-13480, 2009
5) Oshima M, et al：Functional tooth regeneration using a bioengineered tooth unit as a mature organ replacement regenerative therapy. PLoS One 6：e21531, 2011
6) 鷲尾　薫・他：再生医学のいま　基礎研究から臨床への展開に向けて　自己歯根膜細胞シートを用いた歯周病治療．治療 93：2130-2135，2011
7) Yamada Y, et al：Injectable tissue-engineered bone using autogenous bone marrow-derived stromal cells for maxillary sinus augmentation：clinical application report from a 2-6-year follow-up. Tissue Eng Part A 14：1699-1707, 2008
8) Shayesteh YS, et al：Sinus augmentation using human mesenchymal stem cells loaded into a beta-tricalcium phosphate/hydroxyapatite scaffold. Oral Surg Oral Med Oral Pathol Oral Radiol Endod 106：203-209, 2008
9) Murakami S, et al：Regeneration of periodontal tissues by basic fibroblast growth factor. J Periodontal Res 34：425-430, 1999
10) Murakami S：Periodontal tissue regeneration by signaling molecule (s)：what role does basic fibroblast growth factor (FGF-2) have in periodontal therapy? Periodontol 2000 56：188-208, 2011
11) Triplett RG, et al：Pivotal, randomized, parallel evaluation of recombinant human bone morphogenetic protein-2/absorbable collagen sponge and autogenous bone graft for maxillary sinus floor augmentation. J Oral Maxillofac Surg 67：1947-1960, 2009
12) Howell TH, et al：A phase Ⅰ/Ⅱ clinical trial to evaluate a combination of recombinant human platelet-derived growth factor-BB and recombinant human insulin-like growth factor-I in patients with periodontal disease. J Periodontol 68：1186-1193, 1997
13) Iino M, et al：Evaluation of 15 mandibular reconstructions with Dumbach Titan Mesh-System and particulate cancellous bone and marrow harvested from bilateral posterior ilia. Oral Surg Oral Med Oral Pathol Oral Radiol Endod 107：e1-8, 2009
14) Kinoshita K, et al：Promoted new bone formation in maxillary distraction osteogenesis using a tissue-engineered osteogenic material. J Craniofac Surg 19：80-87, 2008
15) Igawa K, et al：Tailor-made tricalcium phosphate bone implant directly fabricated by a three-dimensional ink-jet printer. J Artif Organs 9：234-240, 2006
16) 高戸　毅・他：顎顔面領域における骨・軟骨再生に関する基礎および臨床研究．口科誌 63：207-215，2014
17) Saijo H, et al：Maxillofacial reconstruction using custom-made artificial bones fabricated by inkjet printing technology. J Artif Organs 12：200-205, 2009
18) Izumi K, et al：Development of a tissue-engineered human oral mucosa：from the bench to the bed side. Cells Tissues Organs 176：134-152, 2004
19) Takeuchi J, et al：Clinical evaluation of application of polyglycolic acid sheet and fibrin glue spray for partial glossectomy. J Oral Maxillofac Surg 71：e126-131, 2013
20) Hoshi K, et al：Recent trends in cartilage regenerative medicine and its application to oral and maxillofacial surgery. Oral Sci International 10：15-19, 2013
21) Sakai K, et al：Human dental pulp-derived stem cells promote locomotor recovery after complete transection of the rat spinal cord by multiple neuro-regenerative mechanisms. J Clin Invest 122：80-90, 2012

OPEN ACCESS Freely available online

PLOS | ONE

Axon Diameter and Intra-Axonal Volume Fraction of the Corticospinal Tract in Idiopathic Normal Pressure Hydrocephalus Measured by Q-Space Imaging

Kouhei Kamiya[1,4]*, Masaaki Hori[1], Masakazu Miyajima[2], Madoka Nakajima[2], Yuriko Suzuki[1,3], Koji Kamagata[1], Michimasa Suzuki[1], Hajime Arai[2], Kuni Ohtomo[4], Shigeki Aoki[1]

1 Department of Radiology, Juntendo University Graduate School of Medicine, Tokyo, Japan, **2** Department of Neurosurgery, Juntendo University Graduate School of Medicine, Tokyo, Japan, **3** Philips Electronics Japan, Ltd., Tokyo, Japan, **4** Department of Radiology, Graduate School of Medicine, the University of Tokyo, Tokyo, Japan

Abstract

Purpose: Previous studies suggest that compression and stretching of the corticospinal tract (CST) potentially cause treatable gait disturbance in patients with idiopathic normal pressure hydrocephalus (iNPH). Measurement of axon diameter with diffusion MRI has recently been used to investigate microstructural alterations in neurological diseases. In this study, we investigated alterations in the axon diameter and intra-axonal fraction of the CST in iNPH by q-space imaging (QSI) analysis.

Methods: Nineteen patients with iNPH and 10 age-matched controls were recruited. QSI data were obtained with a 3-T system by using a single-shot echo planar imaging sequence with the diffusion gradient applied parallel to the antero-posterior axis. By using a two-component low-q fit model, the root mean square displacements of intra-axonal space (= axon diameter) and intra-axonal volume fraction of the CST were calculated at the levels of the internal capsule and body of the lateral ventricle, respectively.

Results: Wilcoxon's rank-sum test revealed a significant increase in CST intra-axonal volume fraction at the paraventricular level in patients ($p<0.001$), whereas no significant difference was observed in the axon diameter. At the level of the internal capsule, neither axon diameter nor intra-axonal volume fraction differed significantly between the two groups.

Conclusion: Our results suggest that in patients with iNPH, the CST does not undergo irreversible axonal damage but is rather compressed and/or stretched owing to pressure from the enlarged ventricle. These analyses of axon diameter and intra-axonal fraction yield insights into microstructural alterations of the CST in iNPH.

Citation: Kamiya K, Hori M, Miyajima M, Nakajima M, Suzuki Y, et al. (2014) Axon Diameter and Intra-Axonal Volume Fraction of the Corticospinal Tract in Idiopathic Normal Pressure Hydrocephalus Measured by Q-Space Imaging. PLoS ONE 9(8): e103842. doi:10.1371/journal.pone.0103842

Editor: Christophe Lenglet, University of Minnesota, United States of America

Received February 17, 2014; **Accepted** July 2, 2014; **Published** August 5, 2014

Funding: This study was partly supported by a Research Grant from the Ministry of Health, Labor and Welfare of Japan (2011-Nanchi-018) and a Grant-in-Aid for Scientific Research on Innovative Areas (Comprehensive Brain Science Network) from the Ministry of Education, Science, Sports, and Culture of Japan. The funders had no role in study design, data collection and analysis, decision to publish, or preparation of the manuscript.

Competing Interests: The authors have read the journal's policy and have the following conflicts: Yuriko Suzuki is an employee of Philips Electronics Japan. This does not alter the authors' adherence to PLOS ONE policies on sharing data and materials.

* Email: kkamiya-tky@umin.ac.jp

Introduction

Idiopathic normal pressure hydrocephalus (iNPH) is a clinical entity of unknown cause and is characterized by the triad of gait disturbance, cognitive deterioration, and urinary incontinence [1]. It is also associated with ventricular enlargement, flattening of high-convexity sulci, and periventricular T2-weighted image hyperintensity in the absence of elevated cerebrospinal fluid (CSF) pressure [2]. Gait disturbance is the most frequent symptom of iNPH [3] and is treated by CSF shunting [4]. Although the etiology of gait disturbance in iNPH is not completely understood, a plausible explanation is that the corticospinal tract (CST) is distorted by expansion of the lateral ventricles [1,5,6].

Diffusion tensor imaging (DTI) has been applied to neurological and psychological diseases and is useful to detect brain abnormalities that can not be recognized by conventional T1- or T2-weighted images [7,8]. Previous studies conducted with DTI revealed increases of fractional anisotropy (FA) and axial diffusivity values in the CST in patients with iNPH [9–17], which tended to return to normal after placement of a ventriculoperitoneal (VP) shunt [9–12]. The increases in FA and axial diffusivity have been suggested to result from ventricular enlargement that mechanically compresses the tract and yields more directional water diffusion along it. Diffusion MRI is expected to become a non-invasive method for diagnosing iNPH and predicting the response to surgery [12,17].

Q-space imaging (QSI), a diffusion MRI technique that does not assume that the displacement probability of diffusing water molecules has a Gaussian distribution, can provide quantitative tissue architecture information at cellular dimensions [18–22]. Recently, analysis of axon diameter of neural fibers by using diffusion MRI is becoming a topic for investigation of microstruc-

tural alteration in neurological disease [23–28], although assessment of axonal architecture usually requires high gradient amplitudes and long scanning times, which are not clinically applicable. A two-component low-q fit model for QSI analysis, proposed by Ong et al. [29], enables measurement of the axon diameters of neural fibers with a reasonable scanning time. Briefly, QSI provides a molecular displacement probability density function (PDF), which reflects the axonal architecture, such as axon membranes and myelin sheath acting as barriers to diffusing molecules. In the white matter, the dominant diffusion barrier is the axonal membrane, and the spacing between barriers can be regarded as mean axonal diameter [19]. A two-component low-q fit model used in this study has the following two merits; 1) it accounts for signal from extra- and intra-axonal spaces and has better correlations with pathological findings than a single-component model, 2) it does not require very high gradient amplitudes [29]. The limitation of this method is that it requires prior knowledge of the fiber orientation, because the diffusion gradient must be applied perpendicular to the fiber direction.

The purpose of this study is to investigate alterations in the axonal architecture of the CST in patients with iNPH by using a two-component low-q fit analysis of QSI.

Materials and Methods

Ethics Statement

This study was conducted in accordance with the Declaration of Helsinki and approved by the Institutional Review Board of Juntendo University Hospital and all persons gave their written informed consent prior to their inclusion in the study.

Patients

Nineteen patients with iNPH (10 males and 9 females; 74.3±6.2 years old) and 10 age-matched control subjects (3 males and 7 females; 75.8±5.2 years old) were recruited. Diagnosis of iNPH was made according to the diagnostic criteria of probable iNPH [30]. Those who had a history of neurological disease or any significant findings (as observed on routine MR images) that might affect the brain were excluded. Normal control subjects were required to be >60 years of age and have no neurological or psychological symptoms, history of neurologic diseases, or apparent abnormalities observed on conventional MR images.

QSI data acquisition and processing

QSI data were obtained with a 3-T unit (Achieva, Philips Healthcare, Best, The Netherlands) by using a single-shot echo planar imaging (EPI) sequence. The patient was positioned so that the anterior commissure–posterior commissure (AC-PC) line is parallel to the scanner's x-y plane. The scan parameters were: repetition rate/echo time (TR/TE) = 4500/99 ms, field of view (FOV) = 240×240 mm^2, matrix size = 96×96, slice thickness = 5 mm, 10 axial sections including the level of internal capsule, number of excitations (NEX) = 2, half-Fourier factor = 0.667, 16 b-values (0, 1000, 2000, … 15000 s/mm^2, applied in sequential order), and acquisition time = 828 s. The gradient duration (δ) and time between the two leading edges of the diffusion gradient (Δ) were 39.3 and 48.7 ms, respectively. We did not apply any distortion corrections, because correction was difficult especially at high b values and resulted in severe signal defect in some of the patients.

The two-component low-q fit method for axon diameter analysis necessitates a diffusion gradient perpendicular to the fiber tract to be measured. Ideally, the appropriate direction of diffusion gradient can be determined in each patient by performing tractography of the CST, though it is not realistic in clinical examinations. Instead, we applied diffusion gradient parallel to the antero-posterior axis of the scanner's coordinate system, as the known course of CST [52,53] is substantially perpendicular to the scanner's x-y plane. Examples of the acquired images are shown in Figure 1. By applying the diffusion gradient parallel to the antero-posterior axis, the CST could be identified as a hyperintense tract running from the precentral gyrus to the cerebral peduncle through the posterior limb of the internal capsule [31]. Each ROI was placed manually so that it includes the brightly-appearing CST, using b = 1000~4000 s/mm^2 images. The cranial and caudal sections were also used as references for continuity of the tract. Measurements were performed at two levels. The first section was selected so that it contains the posterior limb of the internal capsule. The second one was selected as two or three sections cranial to the first one, where the CST runs closest to the lateral ventricle. By using in-house software developed in Matlab (R2011b; MathWorks, Natick, MA, USA), the root mean square displacements (RMSDs) of the intra-axonal space (= axon diameter) and intra-axonal volume fraction of the CST were calculated by fitting the echo attenuations (normalized to the maximum value at the q = 0) to equation (1) with a nonlinear least squares algorithm: $E(q) = (1-f_I)\ \exp(-2\pi^2 q^2 Z_E^2) + f_I\ \exp(-2\pi^2 q^2 Z_I^2)$ …(1) where f_I is the relaxation-weighted intra-axonal volume fraction, and Z_E and Z_I are the RMSDs of diffusing molecules in the extra- and intra-axonal spaces, respectively.

Statistical analysis

Statistical analyses were performed by using JMP software (ver. 10.0.2; SAS Institute Inc. Cary, NC, USA). The axon diameter and intra-axonal volume fraction values of the CST from both hemispheres were compared between the patients and controls. To minimize type I errors with multiple comparisons, Bonferroni's correction was applied. The significance level ($p = 0.05$) was therefore reduced to an adjusted p level of 0.006.

Results

Excellent fitting was obtained in all ROIs ($R^2 > 0.95$). Shapiro-Wilk's test was performed to test the hypothesis that the data satisfied Gaussian distribution (the significance level was set at $p = 0.05$). As it was revealed that the assumption of Gaussian distribution was not satisfied in the measurements of axon diameter at the internal capsule level ($p = 0.004$), Wilcoxon's rank-sum test was used for the following group analyses. At the paraventricular level, the CST intra-axonal volume fraction was significantly higher in patients with iNPH than in the controls (right, 0.43±0.04 for the controls, 0.53±0.05 for the patients, $p = 0.0002$; left, 0.43±0.06 for the controls, 0.54±0.06 for the patients, $p = 0.0005$), whereas no significant difference was observed in the CST axon diameter. At the level of the internal capsule, no significant differences were observed between the two groups in either axon diameter or intra-axonal volume fraction (Table 1, Figs. 2, 3). There were no statistically significant differences in ROI sizes between the patients and the controls (Student's t-test; the internal capsule level, 43.6±4.8 mm^2 for the controls and 43.3±7.3 mm^2 for the patients, $p = 0.83$; the paraventricular level, 43.0±9.6 mm^2 for the controls and 41.9±7.4 mm^2 for the patients, $p = 0.66$)

Discussion

A two-component low-q fit analysis of QSI revealed that the CST intra-axonal volume fraction in areas near the ventricles was

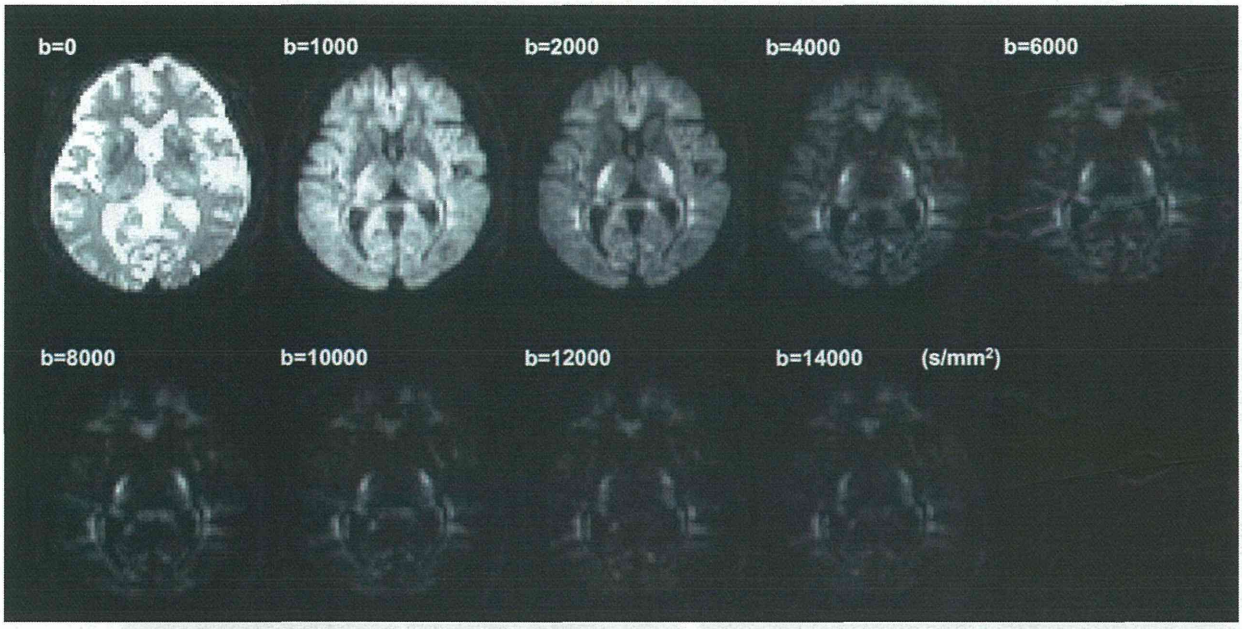

Figure 1. Examples of the acquired diffusion weighted images.
doi:10.1371/journal.pone.0103842.g001

increased in iNPH patients compared with controls, whereas the CST axon diameter was unaltered. Neither CST axon diameter nor intra-axonal volume fraction differed significantly at the level of the internal capsule. Our results are in line with previous DTI studies showing increased diffusion anisotropy of the CST in iNPH, presumably due to compaction of neuronal fibers [9–17]. The increase in CST intra-axonal volume fraction was limited to areas near the lateral ventricle in our study, suggesting that it results from compression by the enlarged ventricles. The unaltered axon diameter of the CST suggests that the iNPH patients involved in this study did not have irreversible axonal damage of the CST.

The exact pathogenesis of the gait disturbance in iNPH is not entirely understood. Though our results suggest that the axons are densely packed in the CST with reduced extra-axonal space, there is no readily available explanation why such situation results in the characteristic gait disturbance in iNPH. A classical hypothesis that remains plausible is that the CST is compressed and/or deformed because of enlargement of the lateral ventricles [1,5,6]. Other pathological changes observed in the brains of patients with iNPH, such as ischemia and gliosis due to transependymal diapedesis of the CSF, may to some extent be related to gait disturbance [32–36]. However, the reversibility of symptoms after shunt surgery even after a long period suggests that irreversible axonal damage is unlikely to be the sole cause of gait disturbance [4]. The "compression hypothesis" is also supported by the fact that the fibers of the legs are closest in proximity to the lateral ventricles [37–39]; this explains why gait disturbance is the most prominent neurological feature in iNPH. Moreover, a detailed tract-specific analysis of the CST demonstrated that the increase in FA was limited to areas near the lateral ventricle [15], an observation consistent with CST compression by the ventricular enlargement.

Analyses of the axon diameter and axon density by using diffusion MRI could have a significant impact on our understanding of white matter architecture and connectivity, neuroanatomical changes that occur in white matter disorders, and changes that occur in white matter during normal and abnormal development. These indices are more straightforward and easier to interpret than other diffusion metrics, such as the mean diffusivity, fractional anisotropy, directional diffusivity, and directional kurtosis, each of which must be interpreted in combination with one or more of the others to understand the microstructural

Table 1. Results of the measurement of CST axon diameter and intra-axonal volume fraction.

	controls		iNPH patients	
	right	left	right	left
Internal capsule level				
axon diameter (μm)	2.07±0.35	2.00±0.31	2.00±0.53	2.16±0.28
intra-axonal volume fraction	0.47±0.05	0.46±0.06	0.49±0.09	0.53±0.08
Paraventricular level				
axon diameter (μm)	2.09±0.12	2.04±0.14	2.10±0.16	2.11±0.15
intra-axonal volume fraction	0.43±0.04	0.43±0.06	0.53±0.05	0.54±0.06

doi:10.1371/journal.pone.0103842.t001

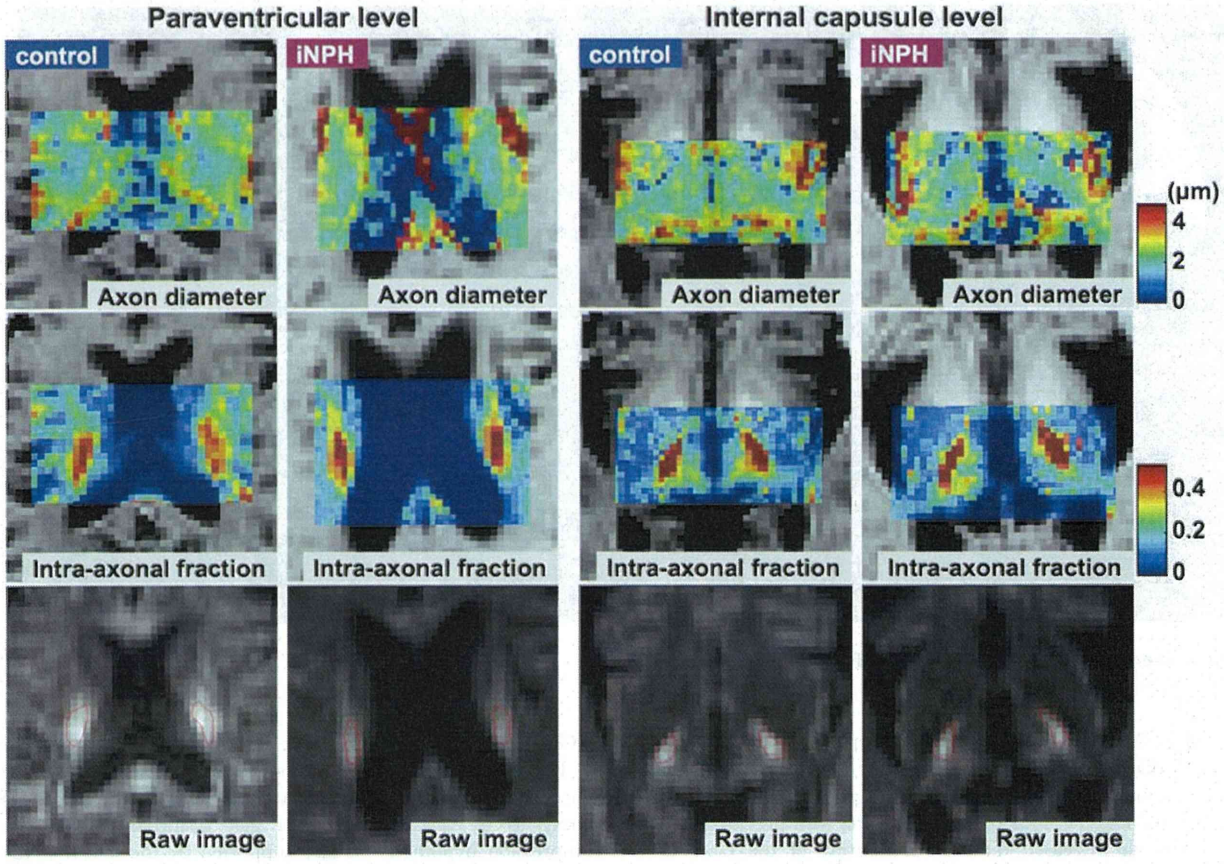

Figure 2. Examples of axon diameter maps (*top row*) and intra-axonal volume fraction maps (*middle row*). ROIs are shown in the raw diffusion image (*bottom row*, b = 2000 s/mm^2).
doi:10.1371/journal.pone.0103842.g002

changes [40,41]. Because axon diameter determines conduction velocity, this metric and the axon density provide information about the role and performance of white matter pathways [42–44]. Axon diameter analysis would also provide a means of testing hypotheses that assume changes in the diameter distribution in diseases such as amyotrophic lateral sclerosis [45], multiple sclerosis [46], and autism [47].

The present results need to be interpreted carefully and hopefully validated by more dedicated experiments, because the short gradient pulse (SGP) approximation ($\Delta >> \delta$) was not satisfied in this study. In principal, SGP approximation needs to be fulfilled for accurate compartment size measurement by QSI. However, with clinical scanners, high q-values can only be obtained with long diffusion gradient pulses because of the relatively weak gradients [20,48,49]. The previous experimental studies reported that the diffraction minima is pushed towards higher q values and the extracted compartment size becomes smaller than the real size when the SGP approximation is violated ($\Delta/\delta \sim 1$) [50]. Though the situation becomes more complicated when there are more than two compartments [50], we speculate that the intra-axonal volume fraction in this study is larger than the real value, as the echo attenuation curve vs q values shifts to the right. Mathematical calibration with the ideal Δ/δ settings [50], or the use of a double-pulsed gradient sequence [51], may be useful to overcome this issue.

The other limitations to this study include the following. First, interpretation of the increase in intra-axonal volume fraction is somewhat ambiguous as it is not directly equal to axonal density. Though we speculate the increased intra-axonal volume fraction reflects that the neural fibers are densely packed with reduced extra-axonal space, other conditions, such as changes in the distribution of axon diameter (i.e, increase of large- and small-diameter axons with few middle-sized axons), may yield similar results. In addition, the intra-axonal volume fraction obtained by the two-component low-q fit method is not completely proven to correlate with that obtained from pathological analyses [29]. Second, the determination of diffusion gradient direction was approximative, and it could have been slightly different from what it should be (perpendicular to the CST). Also, previous DTI studies in iNPH have typically reported increased FA in the CST and decreased FA in the corpus callosum, suggesting regionally dependent microstructural alterations [9,11,13,15]. Therefore, our results require validation by an orientationally invariant method for measuring the axon diameter [25,54]. Lastly, owing to the small sample size and lack of post-operative imaging, the clinical relevance of the QSI measures, such as in monitoring the effect of surgery or pre-operatively predicting the response to surgery, could not be established.

Conclusions

In this study, an analysis of axon diameter and intra-axonal volume fraction demonstrated that in patients with iNPH, the

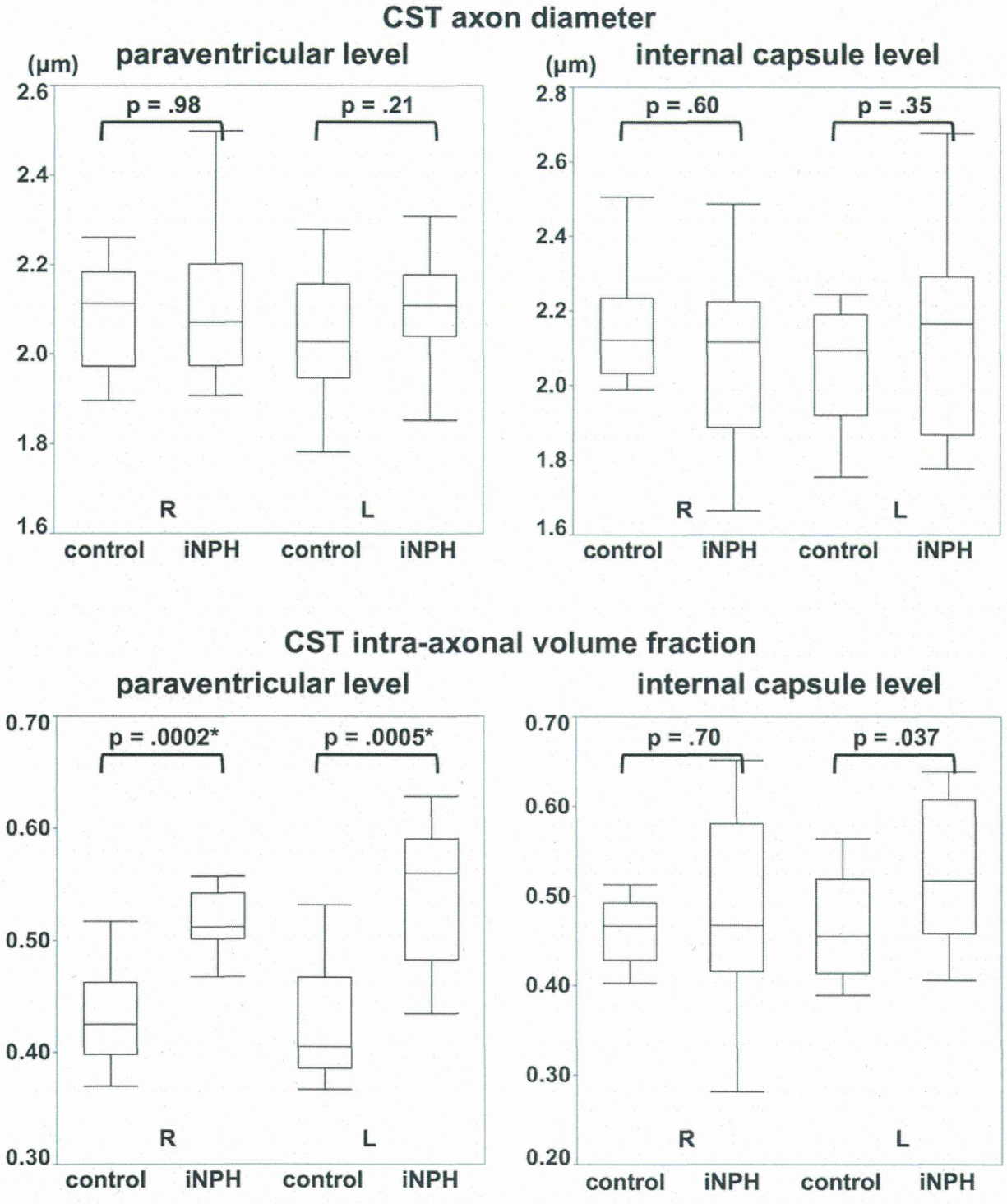

Figure 3. Boxplot comparing the CST axon diameter and intra-axonal volume fraction between the controls and iNPH patients. Statistical analyses revealed a significant increase in CST intra-axonal volume fraction at the paraventricular level in the patients, whereas no significant difference was observed in the axon diameter. At the level of the internal capsule, neither axon diameter nor intra-axonal volume fraction differed significantly between the two groups. * The significance level was set at $p = 0.006$ (Bonferroni's correction for multiple comparison).
doi:10.1371/journal.pone.0103842.g003

CST is compressed by the ventricular enlargement but does not undergo irreversible axonal damage. The axon diameter and intra-axonal volume fraction obtained by QSI yield insights into microstructural alterations in iNPH. Their potential use in predicting the response to surgery or in post-operative monitoring requires further investigation.

Author Contributions

Conceived and designed the experiments: K. Kamiya MH MM MN K. Kamagata HA KO SA. Performed the experiments: K. Kamiya MH MM MN YS K. Kamagata HA MS. Analyzed the data: K. Kamiya MH YS K. Kamagata MS SA. Contributed reagents/materials/analysis tools: MH YS KO SA. Wrote the paper: K. Kamiya MH HA KO SA. Designed the software used in analysis: YS.

References

1. Relkin N, Marmarou A, Klinge P, Bergsneider M, Black PM (2005) Diagnosing idiopathic normal-pressure hydrocephalus. Neurosurgery 57: S4–16; discussion ii–v.
2. Sasaki M, Honda S, Yuasa T, Iwamura A, Shibata E, et al. (2008) Narrow CSF space at high convexity and high midline areas in idiopathic normal pressure hydrocephalus detected by axial and coronal MRI. Neuroradiology 50: 117–122.
3. Marmarou A, Young HF, Aygok GA, Sawauchi S, Tsuji O, et al. (2005) Diagnosis and management of idiopathic normal-pressure hydrocephalus: a prospective study in 151 patients. Journal of Neurosurgery 102: 987–997.
4. Meier U, Lemcke J (2006) Clinical outcome of patients with idiopathic normal pressure hydrocephalus three years after shunt implantation. Acta Neurochir Suppl 96: 377–380.
5. Hakim S, Venegas JG, Burton JD (1976) The physics of the cranial cavity, hydrocephalus and normal pressure hydrocephalus: mechanical interpretation and mathematical model. Surgical Neurology 5: 187–210.
6. Adams RD, Fisher CM, Hakim S, Ojemann RG, Sweet WH (1965) Symptomatic Occult Hydrocephalus with "Normal" Cerebrospinal-Fluid Pressure.A Treatable Syndrome. New England Journal of Medicine 273: 117–126.
7. Shizukuishi T, Abe O, Aoki S (2013) Diffusion tensor imaging analysis for psychiatric disorders. Magnetic resonance in medical science 12: 153–159.
8. Inglese M, Bester M (2010) Diffusion imaging in multiple sclerosis: research and clinical implications. NMR in Biomedicine 23: 865–872.
9. Assaf Y, Ben-Sira L, Constantini S, Chang LC, Beni-Adani L (2006) Diffusion tensor imaging in hydrocephalus: initial experience. AJNR American Journal of Neuroradiology 27: 1717–1724.
10. Jang SH, Ho Kim S (2011) Diffusion tensor imaging following shunt in a patient with hydrocephalus. Journal of Neuroimaging 21: 69–72.
11. Scheel M, Diekhoff T, Sprung C, Hoffmann KT (2012) Diffusion tensor imaging in hydrocephalus–findings before and after shunt surgery. Acta Neurochirurgica 154: 1699–1706.
12. Jurcoane A, Keil F, Szelenyi A, Pfeilschifter W, Singer OC, et al. (2013) Directional diffusion of corticospinal tract supports therapy decisions in idiopathic normal-pressure hydrocephalus. Neuroradiology.
13. Hattingen E, Jurcoane A, Melber J, Blasel S, Zanella FE, et al. (2010) Diffusion tensor imaging in patients with adult chronic idiopathic hydrocephalus. Neurosurgery 66: 917–924.
14. Hattori T, Yuasa T, Aoki S, Sato R, Sawaura H, et al. (2011) Altered microstructure in corticospinal tract in idiopathic normal pressure hydrocephalus: comparison with Alzheimer disease and Parkinson disease with dementia. AJNR American Journal of Neuroradiology 32: 1681–1687.
15. Hattori T, Ito K, Aoki S, Yuasa T, Sato R, et al. (2012) White matter alteration in idiopathic normal pressure hydrocephalus: tract-based spatial statistics study. AJNR American Journal of Neuroradiology 33: 97–103.
16. Nakanishi A, Fukunaga I, Hori M, Masutani Y, Takaaki H, et al. (2013) Microstructural changes of the corticospinal tract in idiopathic normal pressure hydrocephalus: a comparison of diffusion tensor and diffusional kurtosis imaging. Neuroradiology 55: 971–976.
17. Kim MJ, Seo SW, Lee KM, Kim ST, Lee JI, et al. (2011) Differential diagnosis of idiopathic normal pressure hydrocephalus from other dementias using diffusion tensor imaging. AJNR American Journal of Neuroradiology 32: 1496–1503.
18. Cohen Y, Assaf Y (2002) High b-value q-space analyzed diffusion-weighted MRS and MRI in neuronal tissues - a technical review. NMR in Biomedicine 15: 516–542.
19. Assaf Y, Mayk A, Cohen Y (2000) Displacement imaging of spinal cord using q-space diffusion-weighted MRI. Magnetic Resonance in Medicine 44: 713–722.
20. Farrell JA, Smith SA, Gordon-Lipkin EM, Reich DS, Calabresi PA, et al. (2008) High b-value q-space diffusion-weighted MRI of the human cervical spinal cord in vivo: feasibility and application to multiple sclerosis. Magnetic Resonance in Medicine 59: 1079–1089.
21. Farrell JA, Zhang J, Jones MV, Deboy CA, Hoffman PN, et al. (2010) q-space and conventional diffusion imaging of axon and myelin damage in the rat spinal cord after axotomy. Magnetic Resonance in Medicine 63: 1323–1335.
22. Hori M, Fukunaga I, Masutani Y, Taoka T, Kamagata K, et al. (2012) Visualizing non-Gaussian diffusion: clinical application of q-space imaging and diffusional kurtosis imaging of the brain and spine. Magn Reson Med Sci 11: 221–233.
23. Assaf Y, Blumenfeld-Katzir T, Yovel Y, Basser PJ (2008) AxCaliber: a method for measuring axon diameter distribution from diffusion MRI. Magnetic Resonance in Medicine 59: 1347–1354.
24. Dyrby TB, Sogaard LV, Hall MG, Ptito M, Alexander DC (2013) Contrast and stability of the axon diameter index from microstructure imaging with diffusion MRI. Magnetic Resonance in Medicine 70: 711–721.
25. Alexander DC, Hubbard PL, Hall MG, Moore EA, Ptito M, et al. (2010) Orientationally invariant indices of axon diameter and density from diffusion MRI. Neuroimage 52: 1374–1389.
26. Assaf Y, Alexander DC, Jones DK, Bizzi A, Behrens TE, et al. (2013) The CONNECT project: Combining macro- and micro-structure. Neuroimage 80: 273–282.
27. McNab JA, Edlow BL, Witzel T, Huang SY, Bhat H, et al. (2013) The Human Connectome Project and beyond: initial applications of 300 mT/m gradients. Neuroimage 80: 234–245.
28. Morozov D, Bar L, Sochen N, Cohen Y (2013) Modeling of the diffusion MR signal in calibrated model systems and nerves. NMR in Biomedicine 26: 1787–1795.
29. Ong HH, Wehrli FW (2010) Quantifying axon diameter and intra-cellular volume fraction in excised mouse spinal cord with q-space imaging. Neuroimage 51: 1360–1366.
30. Mori E, Ishikawa M, Kato T, Kazui H, Miyake H, et al. (2012) Guidelines for management of idiopathic normal pressure hydrocephalus: second edition. Neurologia Medico-Chirurgica 52: 775–809.
31. Schaefer PW, Grant PE, Gonzalez RG (2000) Diffusion-weighted MR imaging of the brain. Radiology 217: 331–345.
32. Akai K, Uchigasaki S, Tanaka U, Komatsu A (1987) Normal pressure hydrocephalus. Neuropathological study. Acta Pathologica Japonica 37: 97–110.
33. Del Bigio MR (1993) Neuropathological changes caused by hydrocephalus. Acta Neuropathol 85: 573–585.
34. Di Rocco C, Di Trapani G, Maira G, Bentivoglio M, Macchi G, et al. (1977) Anatomo-clinical correlations in normotensive hydrocephalus. Reports on three cases. Journal of the Neurological Sciences 33: 437–452.
35. Bradley WG Jr, Whittemore AR, Watanabe AS, Davis SJ, Teresi LM, et al. (1991) Association of deep white matter infarction with chronic communicating hydrocephalus: implications regarding the possible origin of normal-pressure hydrocephalus. AJNR American Journal of Neuroradiology 12: 31–39.
36. Krauss JK, Regel JP, Vach W, Droste DW, Borremans JJ, et al. (1996) Vascular risk factors and arteriosclerotic disease in idiopathic normal-pressure hydrocephalus of the elderly. Stroke 27: 24–29.
37. Kim JS, Pope A (2005) Somatotopically located motor fibers in corona radiata: evidence from subcortical small infarcts. Neurology 64: 1438–1440.
38. Holodny AI, Gor DM, Watts R, Gutin PH, Ulug AM (2005) Diffusion-tensor MR tractography of somatotopic organization of corticospinal tracts in the internal capsule: initial anatomic results in contradistinction to prior reports. Radiology 234: 649–653.
39. Zolal A, Vachata P, Hejcl A, Bartos R, Malucelli A, et al. (2012) Anatomy of the supraventricular portion of the pyramidal tract. Acta Neurochirurgica 154: 1097–1104; discussion 1104.
40. Jensen JH, Helpern JA (2010) MRI quantification of non-Gaussian water diffusion by kurtosis analysis. NMR in Biomedicine 23: 698–710.
41. Wu EX, Cheung MM (2010) MR diffusion kurtosis imaging for neural tissue characterization. NMR in Biomedicine 23: 836–848.
42. Ritchie JM (1982) On the relation between fibre diameter and conduction velocity in myelinated nerve fibres. Proceedings of the Royal Society of London Series B: Biological Sciences 217: 29–35.
43. Aboitiz F, Scheibel AB, Fisher RS, Zaidel E (1992) Fiber composition of the human corpus callosum. Brain Research 598: 143–153.
44. Lamantia AS, Rakic P (1990) Cytological and quantitative characteristics of four cerebral commissures in the rhesus monkey. Journal of Comparative Neurology 291: 520–537.
45. Cluskey S, Ramsden DB (2001) Mechanisms of neurodegeneration in amyotrophic lateral sclerosis. Molecular Pathology 54: 386–392.
46. DeLuca GC, Ebers GC, Esiri MM (2004) Axonal loss in multiple sclerosis: a pathological survey of the corticospinal and sensory tracts. Brain 127: 1009–1018.
47. Conturo TE, Williams DL, Smith CD, Gultepe E, Akbudak E, et al. (2008) Neuronal fiber pathway abnormalities in autism: an initial MRI diffusion tensor tracking study of hippocampo-fusiform and amygdalo-fusiform pathways. Journal of the International Neuropsychological Society 14: 933–946.
48. Assaf Y, Ben-Bashat D, Chapman J, Peled S, Biton IE, et al. (2002) High b-value q-space analyzed diffusion-weighted MRI: application to multiple sclerosis. Magnetic Resonance in Medicine 47: 115–126.
49. Mayzel-Oreg O, Assaf Y, Gigi A, Ben-Bashat D, Verchovsky R, et al. (2007) High b-value diffusion imaging of dementia: application to vascular dementia and alzheimer disease. Journal of the Neurological Sciences 257: 105–113.
50. Bar-Shir A, Avram L, Ozarslan E, Basser PJ, Cohen Y (2008) The effect of the diffusion time and pulse gradient duration ratio on the diffraction pattern and the structural information estimated from q-space diffusion MR: experiments and simulations. Journal of Magnetic Resonance 194: 230–236.

51. Shemesh N, Ozarslan E, Basser PJ, Cohen Y (2009) Measuring small compartmental dimensions with low-q angular double-PGSE NMR: The effect of experimental parameters on signal decay. Journal of Magnetic Resonance 198: 15–23.
52. Kunimatsu A, Aoki S, Masutani Y, Abe O, Mori H, et al. (2003) Three-dimensional white matter tractography by diffusion tensor imaging in ischaemic stroke involving the corticospinal tract. Neuroradiology 45: 532–535.
53. Yamada K, Kizu O, Kubota T, Ito H, Matsushima S, et al. (2007) The pyramidal tract has a predictable course through the centrum semiovale: a diffusion-tensor based tractography study. Journal of Magnetic Resonance Imaging 26: 519–524.
54. Barazany D, Jones D, Assaf Y (2011) AxCaliber 3D. Proc Int Soc Magn Reson Med 19: 76.

JOURNAL OF MAGNETIC RESONANCE IMAGING 40:1208–1214 (2014)

Original Research

Non-Gaussian Diffusion-Weighted Imaging for Assessing Diurnal Changes in Intervertebral Disc Microstructure

Masaki Katsura, MD, PhD,[1]* Yuichi Suzuki, PhD,[2] Junichi Hata, PhD,[2] Masaaki Hori, MD, PhD,[3] Hiroki Sasaki, MD, PhD,[1] Hiroyuki Akai, MD, PhD,[1] Harushi Mori, MD,[1] Akira Kunimatsu, MD, PhD,[1] Yoshitaka Masutani, PhD,[1] Shigeki Aoki, MD, PhD,[3] and Kuni Ohtomo, MD, PhD[1]

Purpose: To investigate the use of non-Gaussian diffusion-weighted imaging (q-space imaging [QSI]) to estimate diurnal changes in intervertebral disc (IVD) microstructure.

Materials and Methods: IVDs of 15 male subjects (mean age, 27.3 years; mean body mass index, 22.50 kg/m^2) were investigated once in the morning, less than 30 min after rising, and a second time in the evening after at least 10 h of normal physical activity, using 3 Tesla (T) MR imaging. T2 mapping and QSI data values (apparent diffusion coefficient [ADC], root mean square displacement [RMSD], and apparent kurtosis coefficient [AKC]) were calculated and compared between the morning and evening imaging sessions.

Results: The T2, ADC, and RMSD values showed a significant decrease in the evening (175.8 ± 49.5 ms, 1.56 ± 0.32 10^{-3}mm^2/s and 40.0 ± 3.0 μm, respectively; $P < 0.05$ for all values; paired t-test), when compared with the morning values (226.5 ± 83.8 ms, 1.69 ± 0.29 10^{-3}mm^2/s and 45.2 ± 2.9 μm, respectively). The AKC value showed a significant increase in the evening (0.67 ± 0.08), when compared with the morning value (0.58 ± 0.04; $P < 0.05$).

Conclusion: The RMSD and AKC values obtained from QSI analysis may be biomarkers for IVD diurnal microstructural changes.

Key Words: non-Gaussian diffusion-weighted imaging; q-space imaging; intervertebral disc; diurnal changes
J. Magn. Reson. Imaging 2014;40:1208–1214.

THE INTERVERTEBRAL DISC (IVD) consists of the nucleus pulposus (NP) in the core and the annulus fibrosus (AF) at the periphery. The NP is rich in proteoglycans. Proteoglycans interact with hyaluronic acid to form proteoglycan aggregates that are negatively charged and hydrophilic, and which are designed to draw and retain water (1). The AF is composed predominantly of type I collagen organized in dense concentric lamellae forming a fibrous collagen network that maintains the shape of the disc (2).

It has been reported that the spine becomes shorter during the day and recovers during the night (3). This phenomenon has been thought to result from a decrease in disc hydration with daily compression (4). This hypothesis has been supported by several investigators studying morphological aspects of the IVDs, which function to distribute hydraulic pressure under compressive loads (5,6).

Several studies have identified diurnal IVD changes in vivo using magnetic resonance (MR) imaging. Previous investigators reported a decrease in IVD volume (7), and a decrease in NP T2 values (8,9) after a diurnal workload. In addition to morphologic MR imaging, diffusion-weighted imaging (DWI) has also been applied to measure IVD diurnal changes of molecular water diffusion as the apparent diffusion coefficient (ADC) (9). DWI is expected to reflect a microscopic restriction of water molecules and, thereby, microstructural changes such as matrix composition (water, proteoglycan, and collagen) and matrix integrity (9–11).

Conventional DWI analysis is based on an assumption that the water molecules follow a Gaussian distribution. However, human tissue including the IVD is a complex and restricted environment that hinders the

[1]Department of Radiology, Graduate School of Medicine, The University of Tokyo, Tokyo, Japan.
[2]Department of Radiological Technology, The University of Tokyo Hospital, Tokyo, Japan.
[3]Department of Radiology, School of Medicine, Juntendo University, Tokyo, Japan.
Presented in part at the 21st Annual Meeting of the International Society of Magnetic Resonance in Medicine, April 20–26, 2013, Salt Lake City, USA.
*Address reprint requests to: M.K., Department of Radiology, Graduate School of Medicine, The University of Tokyo, 7-3-1 Hongo, Bunkyo-ku, Tokyo 113-8655, Japan.
E-mail: mkatsura-tky@umin.ac.jp
Received October 8, 2012; Accepted September 11, 2013.
DOI 10.1002/jmri.24459
View this article online at wileyonlinelibrary.com.

Table 1.
Morning and Evening T2 Values*

	Morning	Evening	*P* value
ROI 1	67.6 ± 10.5	74.0 ± 14.5	0.08
ROI 2	160.2 ± 53.4	157.0 ± 55.6	0.81
ROI 3	226.5 ± 83.8	175.8 ± 49.5	< 0.01*
ROI 4	146.8 ± 51.9	144.1 ± 49.4	0.69
ROI 5	52.8 ± 7.9	49.9 ± 7.2	0.18

Shown are the results of the T2 value (ms) paired t-test analysis separated for region-of-interest localization. Data are displayed as the mean ± standard deviation. There was a significant decrease in the T2 value in the middle of the nucleus pulposus (ROI 3) in the evening (< 0.05). No significant differences between the morning and the evening were observed in other areas.

distribution of water molecules, resulting in distributions that are far from Gaussian (12). Diffusion signal decay is affected by numerous factors such as water restriction and intra- and extracellular water exchange, as well as variation in tissue compartment sizes. Therefore, different approaches that do not rely on the previously mentioned assumption are required to address all of the factors affecting the signal in diffusion-weighted sequences.

Q-space imaging (QSI) analysis is a more advanced form of diffusion analysis and uses a different approach to measure water molecule diffusion (13,14). In contrast to conventional DWI, QSI does not assume a Gaussian shape for the underlying probability density function (PDF) of water molecule diffusion. It has shown promise for evaluating the microstructure of tissues in vivo (15–18) because it can provide additional diffusion metrics, namely the root mean square displacement (RMSD) and apparent kurtosis coefficient (AKC) (19–22), which give in vivo microstructural information that complements the ADC values. For example, increased ADC can indicate either decreased viscosity of the tissue or spatial dilatation of the water movement space (23). It is difficult to distinguish between these phenomena when using ADC values only. However, the RMSD values reflect the real extent of water molecule movement (13,14). We, therefore, hypothesized that QSI analysis would be able to provide information about IVD diurnal microstructural changes beyond that provided by conventional DWI metrics based on an assumption of a Gaussian shape and model of water molecules.

The purpose of this study is to investigate the use of RMSD and AKC metrics of QSI data to estimate IVD composition diurnal changes.

MATERIALS AND METHODS

Subjects

We investigated 15 male subjects between the ages of 25 and 39 years (mean, 27.3), with a body mass index ranging from 20.06 to 25.56 kg/m^2 (mean, 22.50). We obtained institutional review board ethics approval before initiating the study. All subjects gave written informed consent. Subjects were included if they had no episodes of lower back or radicular pain in the last 6 months. None of the subjects had previous spine surgery, contraindications for MRI, or any previously diagnosed abnormalities of the lumbar spine. They were investigated once in the morning less than 30 min after rising and a second time in the evening after at least 10 h of normal physical activity (office work).

Image Acquisition

All images were acquired using 3 Tesla (T) MR (Signa HDx ver. 14.0; General Electric, Waukesha, WI). After fast spin-echo (FSE) T2-weighted sagittal and axial imaging, QSI and T2 mapping data were acquired in the axial plane of the IVD between the fourth and fifth lumbar vertebrae (L4/5 disc).

FSE T2-weighted images were acquired according to our routine protocol for clinical spine MRI. Imaging parameters for FSE T2-weighted sagittal images were as follows: repetition time (TR): 2740 [ms]; echo time (TE): 106.6 [ms]; number of excitations (NEX): 1.5; field of view (FOV): 28 [cm]; matrix size: 512 × 256; and slice thickness: 3.0 [mm]; imaging time approximately 2.5 min. Imaging parameters for FSE T2-weighted axial images were as follows: TR: 5000 [ms]; TE: 105.1 [ms]; NEX: 0.5; FOV: 25.6 [cm]; matrix size: 256 × 256; and slice thickness: 4.0 [mm]; imaging time approximately 1.5 min. T2-weighted images were not only used for anatomical reference but for the visual Pfirrmann grading of IVDs (24), which was performed by two radiologists (M.K. and A.K., 5 and 17 years of experience, respectively) in consensus.

QSI was performed by using a spin-echo diffusion-weighted echo-planar imaging sequence with the following parameters: TR: 5000 [ms]; TE: 99.6 [ms]; NEX: 3; FOV: 25.6 [cm]; matrix size: 128 × 128; slice thickness: 4.0 [mm]; imaging time approximately 7.5 min; and 11 b values (0, 40, 160, 360, 640, 1000, 1440, 1960, 2560, 3240, 4000 [s/mm^2]) with diffusion encoding in three directions (in the x, y, and z directions,) for every b value. The data from the three directions were acquired separately and then averaged. Corresponding q values for each b value were 59.5, 119.0, 178.6, 238.1, 297.6, 357.1, 416.7, 476.92, 535.7, and 595.2 cm^{-1}, respectively. Gradient length (δ) and the time between the two leading edges of the diffusion gradient (Δ) were 33.9 and 39.9 ms, respectively.

A multiecho spin echo sequence was performed in the axial plane for T2 mapping data acquisition with the following parameters: TR: 1200 [ms]; TE: 7.9,

Table 2.
Morning and Evening ADC Values*

	Morning	Evening	*P* value
ROI 1	0.80 ± 0.18	0.84 ± 0.25	0.58
ROI 2	1.46 ± 0.27	1.45 ± 0.25	0.75
ROI 3	1.69 ± 0.29	1.56 ± 0.32	< 0.01*
ROI 4	1.44 ± 0.28	1.45 ± 0.30	0.61
ROI 5	0.90 ± 0.25	0.85 ± 0.21	0.40

Shown are the results of the ADC value (10^{-3} mm^2/s) paired t-test analysis separated for region-of-interest localization. Data are presented as the mean ± standard deviation. There was a significant decrease in the ADC value in the middle of the nucleus pulposus (ROI 3) in the evening (< 0.05). No significant differences between the morning and the evening were observed in other areas.

Table 3.
Morning and Evening RMSD Values

	Morning	Evening	*P* value
ROI 1	24.4 ± 1.0	24.5 ± 1.1	0.70
ROI 2	37.8 ± 5.2	36.9 ± 5.3	0.51
ROI 3	45.2 ± 2.9	40.0 ± 3.0	< 0.01*
ROI 4	39.5 ± 5.0	39.9 ± 4.6	0.49
ROI 5	26.6 ± 3.0	25.7 ± 1.7	0.35

The results of the RMSD value (μm) paired t-test analysis separated for region-of-interest localization are presented. Data are displayed as the mean ± standard deviation. There was a significant decrease in the RMSD value in the middle of the nucleus pulposus (ROI 3) in the evening (< 0.05). No significant differences between the morning and the evening were observed in other areas.

Table 4.
Morning and Evening AKC Values

	Morning	Evening	*P* value
ROI 1	3.42 ± 0.73	3.27 ± 0.86	0.38
ROI 2	0.71 ± 0.14	0.76 ± 0.20	0.34
ROI 3	0.58 ± 0.04	0.67 ± 0.08	< 0.01*
ROI 4	0.74 ± 0.27	0.69 ± 0.13	0.23
ROI 5	2.86 ± 0.82	2.76 ± 0.82	0.42

The results of the AKC value paired t-test analysis separated for region-of-interest localization are shown. Data are presented as the mean ± standard deviation. There was a significant increase in the AKC value in the middle of the nucleus pulposus (ROI3) in the evening (< 0.05). No significant differences between the morning and the evening were observed in other areas.

15.8, 23.8, 31.7, 39.6, 47.5, 55.4, 63.4 [ms]; NEX: 0.5; FOV: 22 [cm]; matrix size: 256 × 256; slice thickness: 5.0 [mm]; imaging time approximately 2.5 min. This is one of the most common types of sequence for human in vivo spine T2 mapping and was used in a similar manner by other investigators as well (25).

Region of Interest Settings

We decided to measure five equally sized circular regions of interest (ROIs) on the central slice of the axial plane to allow us to evaluate the ROIs in a standardized and reproducible way in accordance with previously published literature (Fig. 1) (9). Each ROI measured 20% of the midline disc diameter (4–6 mm). The ROIs were manually drawn by a radiologist (M.K., 5 years of experience) using T2-weighted axial and sagittal images as an anatomical reference. Structures outside of the IVD, such as cerebrospinal fluid and retroperitoneal tissue, were carefully avoided. It is challenging to clearly define what tissue each ROI represents within the IVD because the transition from AF to NP tissue is usually gradual; however, the most anterior and most posterior ROIs (ROI 1 and ROI 5) were interpreted to represent anterior and posterior AF tissue, respectively. The ROIs in between were interpreted to represent nucleus tissue (ROI 2, anterior NP; ROI 3, middle NP; ROI 4, posterior NP).

Imaging Analysis

T2 maps were created with Functool software (Advantage Windows Workstation, General Electric), and T2 values were measured using the free software Image J (available at: rsbweb.nih.gov/ij/).

Q-space analyses were performed using the free software dTV II FZR and Volume-One 1.72 (Image Computing and Analysis Laboratory, Department of Radiology, The University of Tokyo Hospital, Tokyo, Japan; available at: http://www.ut-radiology.umin.jp/people/masutani/dTV.htm and http://www.volume-one.org/, respectively).

ADC maps (Fig. 2a) based on the conventional mono-exponential model were calculated first. ADC could be calculated by using part of the q-space data because the QSI data included multiple sets of b value data.

Next, the full widths at half maximum (FWHM) of PDF (Fig. 2b) and mean AKC maps (Fig. 2c) were obtained. Detailed new diffusion metrics and their calculation procedures were as previously described (15–22,26). Briefly, the key principle in q-space analysis is that a Fourier transformation of the signal attenuation with respect to q (or the b value) provides the PDF for diffusion by using multiple q values (16). The shape of the computed PDF can be characterized by the FWHM and the maximum height of the curve. In the specific case of an unrestricted Gaussian diffusion, the diffusion constant *D* and the RMSD for one

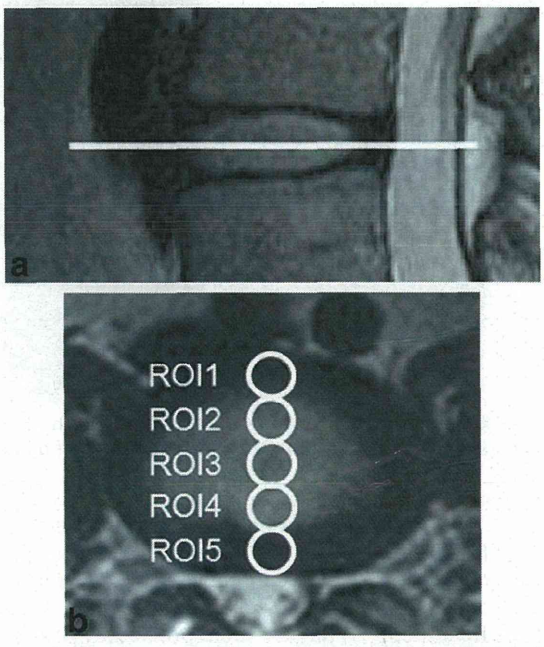

Figure 1. Positioning of the regions of interest (ROIs). The T2-weighted sagittal (a) and axial (b) images were used as anatomical references. Five equally sized circular ROIs (b) were manually drawn on the central slice of the axial planes (a, solid line) by a radiologist (M.K.), and were copied on the T2 maps and q-space images. Each ROI measured 20% of the midline disc diameter in the axial plane. The most anterior and most posterior ROIs (ROI 1 and ROI 5) were interpreted as anterior and posterior AF tissue, respectively. The ROIs in between were interpreted as nucleus tissue (ROI 2, anterior NP; ROI 3, middle NP; ROI 4, posterior NP).

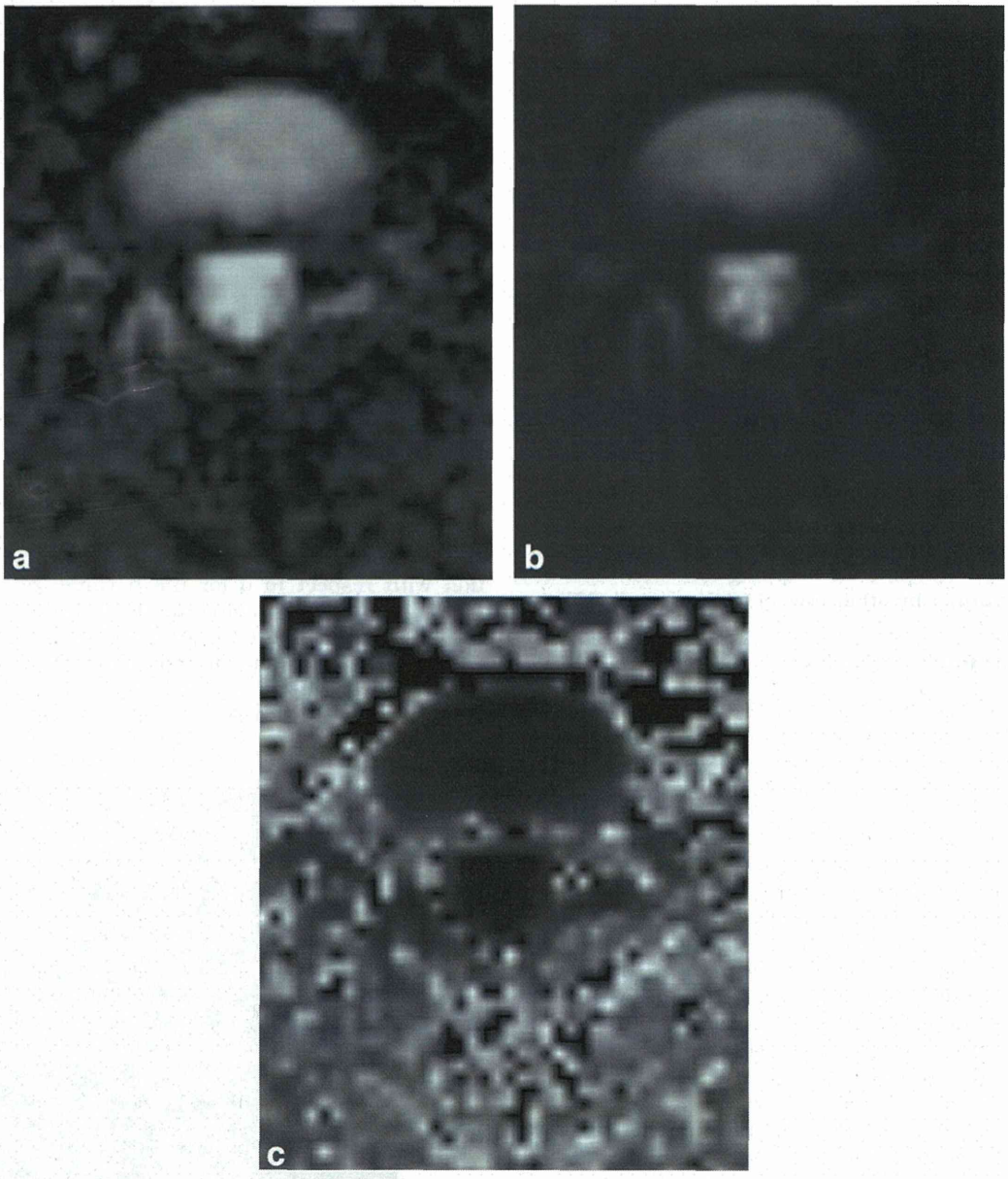

Figure 2. Diffusion metric maps: ADC (a); full width at half maximum of probability density function (b); AKC (c) of the IVD in the axial plane, acquired in the morning from one of the subjects (23-year-old male; body mass index, 21.8).

dimensional diffusion can be computed from the FWHM. Mean RMSD was calculated from the FWHM values (RMSD = 0.425 × FWHM) (17,18). Moreover, the AKC for a single direction can be determined by acquiring data at three or more b values (including b = 0) and fitting them to Eq. [1] as described previously (19):

$$\ln[S(b)]=\ln[S(0)]-bD_{app}+1/6b^2\times D_{app}\times K_{app} \quad [1]$$

where D_{app} is the apparent diffusion coefficient for the given direction and K_{app} is the apparent kurtosis coefficient, which is dimensionless.

Statistical Analysis

The data were analyzed using JMP 9.0.0 software (SAS Institute, Cary, NC). Paired t-tests were applied for assessing significant changes in T2 values and diffusion values (ADC, RMSD, and AKC) between the morning and the evening. A P value < 0.05 was considered to be significant.

RESULTS

The consensus panel classified the L4/5 discs of all subjects as Pfirrmann grade I, meaning there were no degenerative changes (24). T2, ADC, RMSD, and AKC values within each ROI were recorded (data are presented as mean ± standard deviation [SD]) in the morning and in the evening. These values are shown in Tables 1–4 and Figure 3. T2, ADC, and RMSD values showed a significant decrease in the evening (175.8 ± 49.5 ms, 1.56 ± 0.32 $10^{-3}mm^2/s$ and 40.0 ± 3.0 μm,

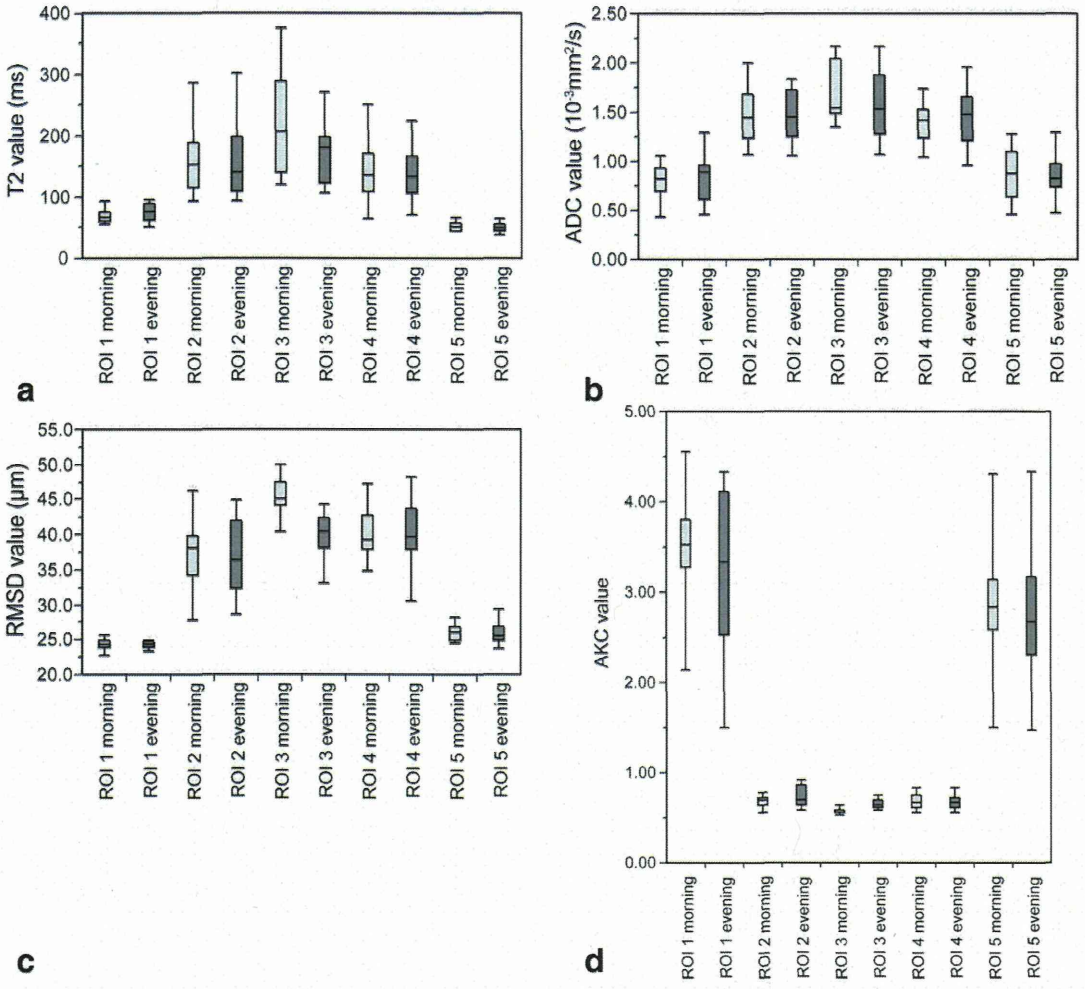

Figure 3. Box plots of T2 (a), ADC (b), RMSD (c), and AKC (d) values within each ROI in the morning and in the evening. Boxes represent the 25th and 75th percentile.

respectively; $P < 0.05$) for all values when compared with the morning values (226.5 ± 83.8 ms, 1.69 ± 0.29 $10^{-3}mm^2/s$ and 45.2 ± 2.9 μm, respectively; $P < 0.05$) in ROI 3 (representing the middle of the nucleus pulposus). In contrast, the AKC value in ROI 3 showed a significant increase in the evening (0.67 ± 0.08), when compared with the morning value (0.58 ± 0.04). No significant differences were observed between the morning and evening in the remaining ROIs.

DISCUSSION

In the present study, changes in T2 values and diffusion metrics of QSI data in IVDs before and after a diurnal load cycle were investigated. T2, ADC, and RMSD metrics in the evening were significantly lower than those in the morning, while the AKC value showed a significant increase in the evening, compared with the morning in the middle of the NP. No significant differences were observed between the morning and the evening in other areas.

Our finding of decreased T2 values after a diurnal load in the middle of the NP is consistent with those of previous reports (8,9). Only Ludescher et al reported on the diurnal ADC value changes of IVD using a 1.5T scanner, which revealed an decrease in the AF and no significant change in the NP (9). However, ADC values from all lumbar IVDs were averaged and analyzed together in their study, and they did not conduct subanalysis at each disc level or in each ROI position (e.g., anterior AF versus posterior AF). Because the compressive force distribution during daily activity should vary according to the disc level and position within each IVD, diurnal changes of diffusion metrics should be analyzed individually.

Our results showed decreased ADC and RMSD values and increased AKC values in the middle of the NP after a diurnal load. Water molecule diffusion is restricted in a complex manner by several factors such as the extracellular matrix (e.g., collagen fibers and proteoglycan) in the IVDs. In general, RMSD is not influenced by the viscosity of water, but by the space for free water movement (13,14). AKC describes the deviation of the water diffusion pattern within a voxel from a Gaussian distribution, which is thought to reflect the changes in microstructural complexity. Our results suggest that compressive forces occurring

during the day cause narrowing of the space for free water movement and a generally higher degree of microstructural complexity, which we are unable to assess with conventional quantitative MR measurements such as T2 or ADC. Diffusion metrics obtained from QSI data may provide additional information with regards to the diurnal microstructural changes occurring in the IVDs, such as matrix composition and integrity.

Several other factors are known to influence IVD quantitative MR measurements, namely, age-related changes and degenerative changes. Previous studies revealed decreasing T2 and ADC values of the NP with increasing age or with progression in the Pfirrmann grade (10,11,24). Karakida et al also found that no significant diurnal T2 value changes could be observed in degenerated discs (8), and they speculated that proteoglycan reduction in the NP with age and disc degeneration reduces not only the capability of holding fluid in the disc, but also the ability to recover the amount of fluid from daily compression force. In the present study, we controlled the age of subjects (mean age of the subjects was 27.3 years), and the degenerative grade of the IVDs (all IVDs included in the study were classified as Pfirrmann grade I, meaning no degenerative changes). Therefore, diurnal changes were investigated with minimal confounding factors. The young and homogenous background of our study group did provide an advantage to minimize potential confounding factors; however, future QSI studies should include assessment of age-related and degenerative changes and various IVD pathologies. QSI may also be applied to assessment of articular cartilage changes. Studies evaluating disc and cartilage changes with different amounts of workload and mechanical stress (e.g., exercise in athletes) with QSI are also awaited. In particular, the potential of QSI as a biomarker for detecting early structural disturbances, when these changes are not visible with conventional MR imaging and before clinical symptoms become evident, should be investigated as well.

One potential limitation of this study is the relatively low maximum b value ($b = 4000$ s/mm^2) that we used to calculate RMSD using q-space analysis. However, using higher b values (or q values) leads to fatal image degradation. We, therefore, decided to evaluate the changes in the RMSD values, rather than the absolute values themselves. Another limitation is partial volume which could have effected on the measurements especially at peripheral part of lumbar disc. However, during ROI selections, structures outside of the IVD, such as cerebrospinal fluid and retroperitoneal tissue, were carefully avoided.

In conclusion, the RMSD and AKC values obtained from QSI analysis may be sensitive biomarkers for IVD diurnal microstructural changes, namely the space for free water movement and microstructural complexity, in which we are unable to assess with conventional diffusion-weighted imaging metrics based on an assumption of a Gaussian shape and model of water molecules. Potentially, this technique can become an appropriate tool to allow characterization of IVD microstructural integrity.

ACKNOWLEDGMENT

Authors state that there is no financial relationship to disclose.

REFERENCES

1. Mwale F, Iatridis JC, Antoniou J. Quantitative MRI as a diagnostic tool of intervertebral disc matrix composition and integrity. Eur Spine J 2008;17(Suppl 4):432–440.
2. Marchand F, Ahmed AM. Investigation of the laminate structure of lumbar disc annulus fibrosus. Spine (Phila Pa 1976) 1990;15:402–410.
3. De Puky P. The physiological oscillation of the length of the body. Acta Orthop Scand 1935;6:338–348.
4. Krag MH, Cohen MC, Haugh LD, Pope MH. Body height change during upright and recumbent posture. Spine (Phila Pa 1976) 1990;15:202–207.
5. Eklund JA, Corlett EN. Shrinkage as a measure of the effect of load on the spine. Spine (Phila Pa 1976) 1984;9:189–194.
6. Reilly T, Tyrell A, Troup JDG. Circadian variation in human stature. Chronobiol Int 1984;1:121–126.
7. Roberts N, Hogg D, Whitehouse GH, Dangerfield P. Quantitative analysis of diurnal variation in volume and water content of lumbar intervertebral discs. Clin Anat 1998;11:1–8.
8. Karakida O, Ueda H, Ueda M, Miyasaka T. Diurnal T2 value changes in the lumbar intervertebral discs. Clin Radiol 2003;58:389–392.
9. Ludescher B, Effelsberg J, Martirosian P, et al. T2- and diffusion-maps reveal diurnal changes of intervertebral disc composition: an in vivo MRI study at 1.5 Tesla. J Magn Reson Imaging 2008;28:252–257.
10. Niu G, Yang J, Wang R, Dang S, Wu EX, Guo Y. MR imaging assessment of lumbar intervertebral disk degeneration and age-related changes: apparent diffusion coefficient versus T2 quantitation. AJNR Am J Neuroradiol 2011;32:1617–1623.
11. Zhang Z, Chan Q, Anthony MP, et al. Age-related diffusion patterns in human lumbar intervertebral discs: a pilot study in asymptomatic subjects. Magn Reson Imaging 2012;30:181–188.
12. Kärger J. NMR self-diffusion studies in heterogeneous systems. Adv Colloid Interface Sci 1985;23:129–148.
13. Cory DG, Garroway AN. Measurement of translational displacement probabilities by NMR: an indicator of compartmentation. Magn Reson Med 1990;14:435–444.
14. Callaghan PT, Coy A, MacGowan D, Packer KJ, Zelaya FO. Diffraction-like effects in NMR diffusion studies of fluids in porous solids. Nature 1991;351:467–469.
15. Assaf Y, Ben-Bashat D, Chapman J, et al. High b-value q-space analyzed diffusion-weighted MRI: application to multiple sclerosis. Magn Reson Med 2002;47:115–126.
16. Farrell JA, Smith SA, Gordon-Lipkin EM, Reich DS, Calabresi PA, van Zijl PCM. High b-value q-space diffusion-weighted MRI of the human cervical spinal cord in vivo: feasibility and application to multiple sclerosis. Magn Reson Med 2008;59:1079–1089.
17. Hori M, Motosugi U, Fatima Z, et al. A comparison of mean displacement values using high b-value Q-space diffusion-weighted MRI with conventional apparent diffusion coefficients in patients with stroke. Acad Radiol 2011;18:837–841.
18. Hori M, Fukunaga I, Masutani Y, et al. New diffusion metrics for spondylotic myelopathy at an early clinical stage. Eur Radiol 2012;22:1797–1802.
19. Jensen JH, Helpern JA, Ramani A, Lu H, Kaczynski K. Diffusional kurtosis imaging: the quantification of non-gaussian water diffusion by means of magnetic resonance imaging. Magn Reson Med 2005;53:1432–1440.
20. Wu EX, Cheung MM. MR diffusion kurtosis imaging for neural tissue characterization. NMR Biomed 2010;23:836–848.
21. Raab P, Hattingen E, Franz K, Zanella FE, Lanfermann H. Cerebral gliomas: diffusional kurtosis imaging analysis of microstructural differences. Radiology 2010;254:876–881.
22. Jensen JH, Falangola MF, Hu C, et al. Preliminary observations of increased diffusional kurtosis in human brain following recent cerebral infarction. NMR Biomed 2011;24:452–457.
23. Clark CA, Le Bihan D. Water diffusion compartmentation and anisotropy at high b values in the human brain. Magn Reson Med 2000;44:852–859.

24. Pfirrmann CW, Metzdorf A, Zanetti M, Hodler J, Boos N. Magnetic resonance classification of lumbar intervertebral disc degeneration. Spine (Phila Pa 1976) 2001;26:1873–1878.
25. Stelzeneder D, Welsch GH, Kovacs BK, et al. Quantitative T2 evaluation at 3.0T compared to morphological grading of the lumbar intervertebral disc: a standardized evaluation approach in patients with low back pain. Eur J Radiol 2012; 81:324–330.
26. Hori M, Fukunaga I, Masutani Y, et al. Visualizing non-Gaussian diffusion: clinical application of q-space imaging and diffusional kurtosis imaging of the brain and spine. Magn Reson Med Sci 2012;11:221–233.

ORIGINAL RESEARCH

Reduction of false positives at vessel bifurcations in computerized detection of lung nodules

Yukihiro Nomura[1], Mitsutaka Nemoto[1], Yoshitaka Masutani[2], Shouhei Hanaoka[3], Takeharu Yoshikawa[1], Soichiro Miki[1], Eriko Maeda[1], Naoto Hayashi[1], Naoki Yoshioka[4], Kuni Ohtomo[3]

1. Department of Computational Diagnostic Radiology and Preventive Medicine, the University of Tokyo Hospital, Tokyo, Japan. 2. Graduate School of Information Sciences, Hiroshima City University, Hiroshima, Japan. 3. Department of Radiology, the University of Tokyo Hospital, Tokyo, Japan. 4. Department of Radiology, Sanno Hospital, Tokyo, Japan.

Correspondence: Yukihiro Nomura. Address: Department of Computational Diagnostic Radiology and Preventive Medicine, The University of Tokyo Hospital, 7-3-1 Hongo, Bunkyo-ku, Tokyo 113-8655, Japan. E-mail: nomuray-tky@umin.ac.jp

Received: April 3, 2014 **Accepted:** July 4, 2014 **Online Published:** July 15, 2014
DOI: 10.5430/jbgc.v4n3p36 **URL:** http://dx.doi.org/10.5430/jbgc.v4n3p36

Abstract

Objective: We describe a new false positive (FP) reduction method based on surface features in our computerized detection system for lung nodules and evaluate the method using clinical chest computed tomography (CT) scans.

Methods: In our detection method, nodule candidates are extracted using volumetric curvature-based thresholding and region growing. For various sizes of nodules, we adopt multiscale integration based on Hessian eigenvalues. For each nodule candidate, two surface features are calculated to differentiate nodules and FPs at vessel bifurcations. These features are fed into a quadratic classifier based on the Mahalanobis distance ratio.

Results: In an experimental study involving 16 chest CT scans, the average number of FPs was reduced from 107.5 to 14.1 per case at 90% sensitivity.

Conclusions: This proposed FP reduction method is effective in removing FPs at vessel bifurcations.

Key words

Surface feature, Vessel bifurcation, Lung nodule, Chest CT, Computer-assisted detection

1 Introduction

Lung cancer is one of the most difficult cancers to cure, and early detection is necessary to improve patient outcomes [1, 2]. Chest computed tomography (CT) can help detect lung cancer at an earlier stage than chest radiography [3]. The recent development of multidetector-row CT (MDCT) has allowed the acquisition of thin-section images of a whole lung during a single breath hold [4]. However, due to the large number of images generated by chest MDCT examination, reading by radiologists is time-consuming and may result in missed nodules. Therefore, computer-assisted detection (CAD) systems for lung nodules in chest CT images have been developed to assist radiologists.

A number of research groups have reported a variety of CAD systems for detecting lung nodules in chest CT images, including multiple grayscale thresholding [5, 6], local density maximum algorithm [7], fuzzy clustering [8], genetic algorithm